

Indicator Dilution Models for the Quantification of Microvascular Blood Flow With Bolus Administration of Ultrasound Contrast Agents

Costas Strouthos, Marios Lampaskis, Vassilis Sboros, Alan McNeilly,
and Michalakis Averkiou, *Member, IEEE*

Abstract—Indicator dilution methods have a long history in the quantification of both macro- and microvascular blood flow in many clinical applications. Various models have been employed in the past to isolate the primary pass of an indicator after an intravenous bolus injection. The use of indicator dilution techniques allows for the estimation of hemodynamic parameters of a tumor or organ and thus may lead to useful diagnostic and therapy monitoring information. In this paper, we review and discuss the properties of the lognormal function, the gamma variate function, the diffusion with drift models, and the lagged normal function, which have been used to model indicator dilution curves in different fields of medicine. We fit these models to contrast-enhanced ultrasound time-intensity curves from liver metastases and the ovine corpora lutea. We evaluate the models' performance on the image data and compare their predictions for hemodynamic-related parameters such as the area under the curve, the mean transit time, the full-width at half-maximum, the time to the peak intensity, and wash-in time. The models that best fit the experimental data are the lognormal function and the diffusion with drift.

I. INTRODUCTION

WITH the introduction of microbubble contrast agents, ultrasound imaging at low mechanical index (MI) with real-time scanning has been successfully used to detect blood flow at both macro- and micro-circulation levels [1]. This important development in medical imaging is attributed to certain key features of the microbubbles. Because the contrast microbubbles are comparable in size with red blood cells, they do not diffuse or leak out of the vascular compartment, and behave as pure blood-tracers. They also increase the image contrast of the blood when visualized with specific non-linear imaging methods [2]–[5]. Contrast-enhanced ultrasound (CEUS) has been successfully applied in oncological radiology to detect and characterize liver [6], [7], prostate [8], [9], kidney [10], and breast [11] lesions.

The microbubbles may be introduced into the body either as a bolus injection or as a constant infusion. With a bolus injection, it is customary to use low MI real-time imaging and form curves of image intensity as a function of time (time-intensity curves) for quantification of blood flow in a region of interest (ROI). With a constant infusion, a destruction-replenishment protocol is usually followed for the quantification of blood flow, where the bubbles are destroyed in a plane (creating a negative bolus) and the wash-in of bubbles from the surrounding area is monitored [12]. The bolus injection is sometimes preferred to constant infusion, because, in the latter, a larger amount of indicator is needed, it takes the indicator a long time to reach steady state, and the infusion set-up adds further complexity (tubing, control of flow rates, amount to inject, agitation of contrast solution). This paper focuses on the bolus injection method. The destruction-replenishment technique will be discussed in a future article.

The use of indicator dilution techniques in clinical applications has a long history. Stewart [13] introduced this technique at the end of the nineteenth century by infusing an indicator intravenously at a constant rate to study the cardiac output. A bolus injection method for measuring the cardiac output was introduced by Henriques [14] at the beginning of the twentieth century, who also noticed that the indicator started to recirculate before the primary pass was complete. Subsequently, several authors used indicator dilution techniques in various applications. For early works in the field see [15]–[22]. Indicator dilution methods have been used extensively in radiological applications such as ultrasound [23], scintigraphy [24], magnetic resonance imaging [25], and computed tomography [26].

Often, CEUS time-intensity curves are noisy and the wash-out tail is affected by the recirculation of the microbubbles. At moderate microbubble concentrations, acoustic shadowing effects are negligible and the back-scattered acoustic intensity I is directly proportional to the concentration [27]–[29]. Therefore, one can employ theoretical models based on indicator dilution techniques for ultrasound contrast agents to curve-fit the data to suppress noise and isolate the primary pass. This approach also allows an analytical determination of important hemodynamic-related parameters such as the area under

Manuscript received August 12, 2009; accepted March 17, 2010.

C. Strouthos, M. Lampaskis, and M. Averkiou are with the University of Cyprus, Department of Mechanical and Manufacturing Engineering, Nicosia, Cyprus.

V. Sboros is with the University of Edinburgh, Division of Medical Physics, Edinburgh, UK.

A. McNeilly is with the Medical Research Council Human Reproductive Sciences Unit, Centre for Reproductive Biology, Edinburgh, UK.

Digital Object Identifier 10.1109/TUFFC.2010.1550

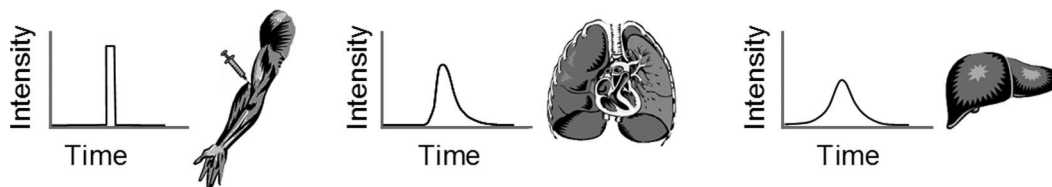


Fig. 1. Schematic representation of the changes in the shape of a time-intensity curve during passage of the indicator from the injection point through the heart and lungs to the liver or other organ or tissue with a microvascular structure.

the time-intensity curve (AUC), the mean transit time (MTT), and the time to the peak intensity (t_p) [30]–[32], which are related to blood flow and blood volume in an ROI. This approach leads to more accurate results than simple smoothing techniques which are often used to exclude outliers from the data, but cannot be used to eliminate the effects of recirculation. In the field of CEUS, indicator dilution techniques have been used in cardiology [27], [33]–[35], the microcirculation of an exteriorized cremaster muscle [36], brain perfusion [37]–[38], and tissue-mimicking flow phantom experiments [39].

The objective of this work is twofold: First, to provide a detailed review of the physical and physiological basis of various models based on the indicator dilution theory after a bolus of contrast is injected intravenously, and second, to evaluate the performance of the models on CEUS data from the microcirculation in the ovine corpus luteum and liver metastases.

This paper is organized as follows. Section II first reviews the basics of the indicator dilution theory based on intravenous bolus injection of an indicator. Then, the properties of the most commonly used indicator dilution models are reviewed. More specifically, the lognormal model, the Erlang and gamma variate models, the diffusion with drift models, and the lagged normal model are discussed. In Section III, the imaging protocol and the imaging quantification methods are presented. In Section IV, the results from curve-fitting the models to CEUS time-intensity curves from human liver metastases and the ovine corpora lutea are presented. Finally, in Section V the results are discussed and the conclusions are presented in Section VI.

II. INDICATOR DILUTION METHODS AND THEORETICAL MODELS

The indicator particles after an instantaneous bolus injection traverse an ROI at different times, because they are dispersed through branching vessels, or because of Brownian motion, laminar flow, or turbulence. This is shown schematically in Fig. 1, where a short rectangle-shaped bolus of indicator approaching a delta function spreads in time after its transit through different organs. Even though the initially injected delta-function-shaped bolus of indicator has spread to a certain degree, it is often approximated as the initial input to an ROI. Therefore, an indicator dilution curve is interpreted as the probability

density function of the indicator transit times through the system; that is, it may be related to the amount of indicator particles traversing an ROI per unit time.

If the amount of the indicator m in a bolus injection is known, and the indicator concentration as a function of time is measured in an ROI, then both the volumetric blood flow rate (F) and the blood volume (V) can be calculated in terms of AUC and MTT:

$$F = m \cdot (\text{AUC})^{-1} \quad (1a)$$

$$V = F \cdot \text{MTT}. \quad (1b)$$

These relations are known as the Stewart-Hamilton relations [13]–[15] and their derivation makes no assumptions about the shape of the indicator dilution curves. In CEUS, the backscattered intensity $I(t)$ is measured instead of the microbubbles concentration, therefore F and V cannot be measured directly. However, as mentioned in Section I, the backscattered intensity is proportional to the concentration at low microbubble concentrations [27]–[29], implying that one can measure quantities that are proportional to F and V from (1a) and (1b). At large blood flow rates the microbubbles move quickly into an ROI, implying a short t_p , and vice versa [40]. Therefore, in highly vascularized malignant tumors, where the blood flow rate is large, we expect a shorter rise in the time-intensity curve as compared with the normal parenchyma. It is also noted that t_p is usually not affected by indicator recirculation, because it is shorter than the systemic recirculation time.

The validity of the Stewart-Hamilton relations is based on various assumptions, most of them discussed by Zierler [22]. The mass conservation principle is a basic assumption of indicator dilution methods. However, this assumption is usually not valid in practice, because a large fraction of the indicator gets lost in the body before it reaches a given ROI (e.g., natural deterioration of microbubbles [29], the filtering effect through the transpulmonary circulation). However, the relations of (1) still hold in a relative sense. Other assumptions made in most clinical applications are:

- The system is a compartment with a single input and a single output.
- The injection of the indicator is instantaneous, i.e., it can be approximated by a Dirac delta function. This assumption is sufficiently accurate if the MTT through the system is much larger than the injection time, otherwise (1b) is not valid, although (1a) remains valid.

To avoid the assumption of an instantaneous bolus injection, some authors employed deconvolution techniques to estimate the system's transfer function after measuring both the input and output time-intensity curves [39].

- The blood flow rate is constant (valid only for certain families of vessels; also fairly true if the measurement time is made short enough).
- The system is stationary, that is, the distribution of transit times in an ROI does not change during the experiment (remains valid in pulsatile systems provided that the changes in transit times fluctuate faster about some mean value than the evolution of the dilution curve). Also the blood flow in the body is not disturbed by the injection of the indicator (valid in most cases because the amount of the injected indicator is very small compared with the overall blood volume).
- The vessels have fixed sizes and the blood is an incompressible fluid.
- The distribution of transit times of the indicator is identical with the distribution of transit times of the blood [a complete mixing of the agent in blood, such as in the right heart, is sufficient for the application of (1a)].

In the following subsections, we present in detail the physical and physiological basis of the lognormal function, the Erlang and gamma variate functions, the diffusion with drift models, and the lagged normal function. We also show that advantage can be taken from the convenient mathematical properties of the models to calculate, in most cases analytically, hemodynamic-related parameters such as AUC, t_p , and MTT directly from the models' parameters.

A. The Lognormal Function

It is well known from statistics that a variable has a lognormal distribution if it results from the product of a large number of independent random variables. The lognormal distribution function with a delay t_0 is given by

$$I(t) = \frac{\text{AUC}}{\sqrt{2\pi\sigma}(t - t_0)} e^{(\ln(t-t_0)-\mu)^2/(2\sigma^2)} + I_0, \quad \text{with } t > t_0, \quad (2)$$

where $I(t)$ is the backscattered signal intensity (which is proportional to the indicator concentration) as a function of time. The variables μ and σ are the mean and standard deviation of the normal distribution of the logarithm of the independent variable t . The curve can be scaled horizontally by varying μ and can become more skewed by increasing σ . The baseline intensity I_0 is essentially an intensity offset (DC offset) because of the noise level present in the image and any linear signal caused by incomplete cancellation in the nonlinear pulsing scheme. The inclusion of I_0 in (2) applies specifically to ultrasound time-intensity and is not part of the original statistical model.

The estimated bolus arrival time is set to zero by truncating the data and resetting the values of t accordingly. The parameter t_0 is a small adjustment to the time origin of the distribution which is obtained from the fitting algorithm outlined in detail in Section III-B. This parameter is needed because of the difficulty of accurately identifying the time of the first arrival of contrast, as a result of the small signal-to-noise ratio before bubble arrival in the ROI. The definitions of I_0 and t_0 have similar meanings in the other models of $I(t)$ hereafter. In [41], Arditi *et al.* presented a transformation for converting (2) into a lognormal distribution of the flow velocity. MTT, defined as the first moment of the probability density function ($I(t) - I_0$) minus the bolus arrival time t_0 , and t_p are given by

$$\text{MTT} = e^{\mu + \sigma^2/2}, \quad t_p = e^{\mu - \sigma^2}. \quad (3)$$

Example curves from (1) (with $I_0 = 0$) normalized to unit peak intensity are shown in Fig. 2(a). For fixed μ , the curves become more skewed as σ increases (i.e., with a faster wash-in rate and a slower wash-out rate). For fixed σ and increasing μ , the curves are shifted to the right and they become broader with slower wash-in and wash-out rates.

Koch [42], [43] presented several examples of lognormal distributions in biological sciences. The importance of the lognormal distribution in sciences including biosciences has been also emphasized by Limpert *et al.* [44]. Since the middle of the twentieth century, the lognormal function has been used by various groups as an empirical model for fitting indicator dilution curves. Stow and Hetzel [45] suggested that after omitting the effects of recirculation, an indicator dilution curve resulting from a bolus injection approximates a lognormal distribution. Wise [46] realized that the single exponential extrapolation of the wash-out part of indicator dilution curves suggested by Hamilton *et al.* [16] does not adequately isolate the primary pass and he suggested that the lognormal distribution is a more appropriate model, because its down-limb curve falls more rapidly than the single exponential. More precisely, Wise [46] approximated the lognormal curve with two straight lines, the tangents at its points of inflection, and he derived the parameters that characterize it from the triangle formed by these two tangents and the base line. Later, Linton *et al.* [47] and Band *et al.* [48] employed the lognormal distribution as an indicator dilution model to fit the primary pass of indicator dilution curves in measurements of the cardiac output and showed that in this way one can avoid overestimates inherent in treating the wash-out as a single exponential decay.

The importance of the lognormal function in the perfusion of regularly perfused organs has been emphasized in a more recent analytical work by Qian and Bassingthwaite [49]. These authors studied the distribution of blood flow and the kinetics of indicator wash-out in the stochastic flow bifurcation model originally developed by Van Beek *et al.* [50]. The model assumes that each parent vessel generates two daughter vessels with a fraction γ of the flow in

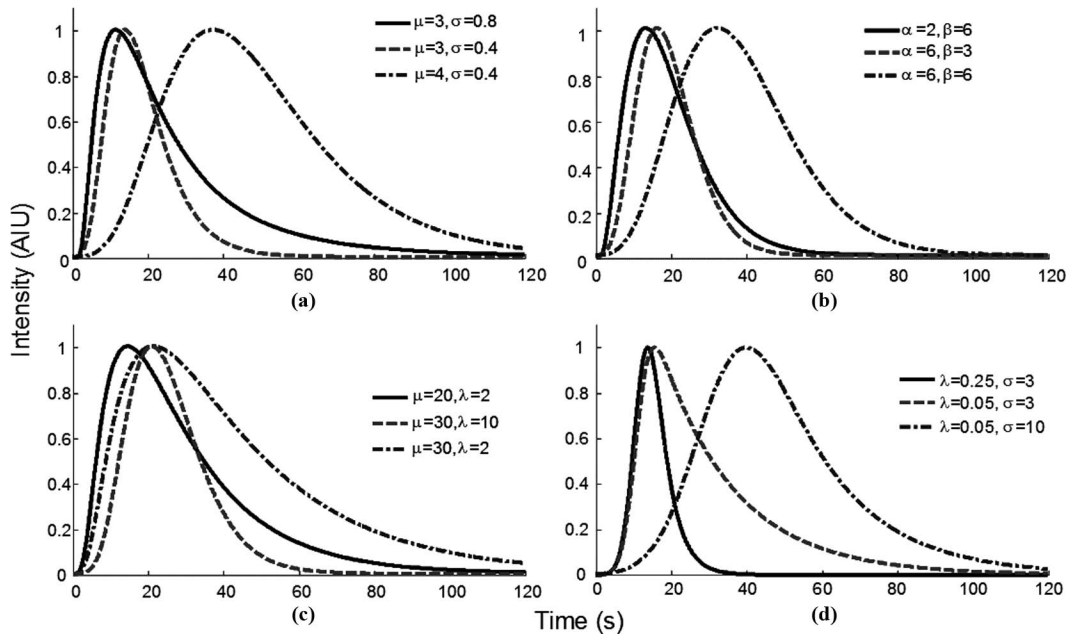


Fig. 2. Plots of four models with important parameters varied: (a) the lognormal function, (b) the gamma variate function, (c) the local density random walk function, (d) the lagged normal function with one exponential. All curves are normalized with respect to their maximum.

the parent vessel entering one branch and the remaining fraction entering the other. Qian and Bassingthwaite assumed that γ is a random variable ($0 \leq \gamma \leq 1$) with an arbitrary probability density function and showed that, for a network of vessels with a large number of generations, the flow distribution is a lognormal function and the relative dispersion (standard deviation divided by the mean) of the blood flow exhibits fractal scaling. They also showed that the large time asymptotic behavior of the tracer dilution curve is well represented by a lognormal distribution function.

In the field of CEUS, the lognormal function was employed by Tiemann *et al.* [27] to fit time-intensity curves from phantom experiments and an *ex vivo* beating heart model. This work was done using harmonic power Doppler imaging (H-PDI) with an HDI-3000 (ATL Ultrasound Inc., Bothell, WA), a technique that uses high MI (thus causing bubble destruction) with intermittent scanning at 1 Hz. These authors measured the AUC of time-intensity curves for different contrast dosages at a constant flow rate and showed that there is a linear relationship between the AUC and the contrast dosage. This result is in agreement with (1a) for injections with less than 420 mg of Levovist, i.e., below the shadowing onset. Furthermore, by comparing the MTT measured from CEUS time-intensity curves and indocyanine green dilution curves, the authors concluded that Levovist microbubbles at moderate concentrations are free-flowing tracers through the myocardium.

B. The Erlang and Gamma Variate Functions

The Erlang probability density function is derived by assuming that constant blood flow can be modeled as a series of n mixing homogeneous compartments of equal

volume V_c , with each compartment having only one input and one output of blood [51], [52]. After an instantaneous injection of an indicator bolus, the rate of change of the indicator concentration $C_i(t)$ in compartment i ($i = 1, \dots, n$) is given by the following set of differential equations:

$$\frac{dC_1}{dt} = \frac{m}{V_c} \delta(t) - \frac{F}{V_c} C_1 \quad (4a)$$

$$\frac{dC_i}{dt} = \frac{F}{V_c} [C_{i-1}(t) - C_i(t)], \quad i = 2, \dots, n, \quad (4b)$$

where $\delta(t)$ is the Dirac delta function. The validity of (4a) and (4b) is based on the assumptions that there is complete mixing between the indicator particles and the blood in each compartment, and the indicator movement from one compartment to the next is unidirectional, i.e., the diffusion process is neglected. The single-compartment solution of (4a) is a single-exponential decay, which is what Hamilton *et al.* [16] used to fit the wash-out part of indicator dilution curves. After the system of differential equations (4a) and (4b) is solved, we obtain $C_n(t)$ which, as stated earlier, is linearly proportional to $I(t)$,

$$I(t) = \frac{\text{AUC}}{\beta^n (n-1)!} (t - t_0)^{n-1} e^{-(t-t_0)/\beta} + I_0. \quad (5)$$

The function $(I(t) - I_0)$ is known as the Erlang probability density function with a delay t_0 . The parameter $\beta \equiv V_c/F$ is called the rate parameter, because it is equal to the time constant of a single compartment's response to an impulse bolus. The number of compartments n is also known as the shape parameter because the skewness of the distribution is equal to $2/\sqrt{n}$ implying that $I(t)$ becomes more symmetric as the number of compartments increases. This is expected because the indicator bolus

becomes more dispersed as it passes through a large number of compartments.

Linton *et al.* [47] compared the Erlang function with the lognormal function by fitting data generated by (5) for a range of skewness found in human indicator dilution curves and concluded that, for practical purposes, the lognormal and Erlang functions give very similar results. The main difference between the two functions is that, for highly skewed Erlang functions (i.e., small number of compartments), the lognormal curves are more rounded near the origin.

An alternative to the deterministic approach discussed previously, a stochastic derivation of the Erlang function as an indicator dilution model, was recently given by Mischi *et al.* [35]. In [35], a random variable is associated with the position of the indicator particle along the tube. When the probability associated with the movement of the particle to the subsequent section of the tube (compartment) is small, a Poisson distribution can represent the indicator concentration resulting from the unidirectional movement of the indicator particles from one section of the tube to the next. As a result of this stochastic process, Mischi *et al.* [35] showed that the Erlang function represents the impulse response function of the system.

One can also relax the constraint of an integer number of compartments and obtain the gamma variate function given by [53]

$$I(t) = \frac{\text{AUC}}{\beta^{\alpha+1}\Gamma(\alpha+1)}(t-t_0)^\alpha e^{-(t-t_0)/\beta} + I_0, \quad (6)$$

where $\alpha \equiv n - 1$. The term $\beta^{\alpha+1}\Gamma(\alpha+1)$ normalizes the gamma variate in (6) so that $(I(t) - I_0)$ is a probability distribution that integrates to unity when AUC equals 1. Advantage can be taken of the convenient properties of the gamma variate function to calculate the MTT and t_p :

$$\text{MTT} = \beta(\alpha+1), \quad t_p = \alpha \cdot \beta. \quad (7)$$

Example curves from (6) (with $I_0 = 0$) normalized to unity peak intensity are shown in Fig. 2(b). As the parameter α increases for fixed β , the curves become more symmetric (less skewed), for the same reasons as explained above for the Erlang function. For fixed α , as the rate parameter β increases, both the wash-in and wash-out rates increase. As discussed by Thompson *et al.* [53] and Li *et al.* [54], the nonlinear dependency of the parameters in (6) needs to be taken into account in the non-linear regression to obtain unbiased estimates of AUC, β , and α . In this paper, the gamma variate function is used instead of the Erlang function to fit experimental data; the gamma variate function is more general because it allows for non-integer values of the parameter α .

The gamma variate function can be extended to accommodate compartments of unequal volumes [55]. In this case, the solution for n compartments is a summation of n single exponentials whose coefficients depend on the different volumes of the compartments. However, the rapidly

increasing number of fitting parameters in this case does not lead to an improved representation of real tracer dilution curves.

The simplicity of the gamma variate function motivated various groups to employ it for fitting CEUS time-intensity curves. In an *in vitro* study, Li and Yang [39] employed the gamma variate function to fit time-intensity curves for constant and pulsatile flow. These authors determined the values of the parameters α and β by fitting the gamma variate function to their data. By using deconvolution methods, the authors also extracted the transfer function of the phantom and showed that this method is effective for both constant and pulsatile flows. The two-compartment gamma variate function was employed by Wasmeier *et al.* [34] to fit time-intensity curves from images of rats' myocardium. These authors showed that with CEUS they could differentiate between infarcted and non-infarcted myocardial segments. In all of these cases, however, the non-linear dependency of the parameters in (6) was not properly taken into account, which might have resulted in biased estimates of the fitted parameters.

C. Diffusion With Drift Models

Sheppard and Savage [56] were the first to suggest the application of diffusion with drift models for the interpretation of indicator dilution curves. The movement of indicator particles through part of the circulation system is regarded as a longitudinal diffusion superimposed on a linear convection. The equation that describes the diffusive and convective transport is given by

$$\frac{\partial C(x,t)}{\partial t} = D \frac{\partial^2 C(x,t)}{\partial x^2} - v \frac{\partial C(x,t)}{\partial x}, \quad (8)$$

where $C(x,t)$ is the indicator concentration at position x and time t , D is the effective longitudinal diffusion coefficient, and v is the blood velocity. In complicated systems such as the blood flow in tumor microcirculation, D is a collective parameter that represents contributions from various physical mechanisms such as turbulent mixing, Brownian motion, and transport in a microvascular bed with diffusive architecture.

Norwich and Zelin [57] solved (8) for an instantaneous impulse bolus injection in the case of no special boundary condition at the outlet to obtain $C(x,t)$ which is linearly proportional to backscattered signal intensity in CEUS, $I(t)$, given by

$$I(t) = \text{AUC} \cdot \left(\frac{e^\lambda}{\mu} \right) \sqrt{\frac{\mu}{(t-t_0)2\pi}} \cdot \exp \left[-\frac{1}{2} \lambda \left(\frac{\mu}{(t-t_0)} + \frac{(t-t_0)}{\mu} \right) \right] + I_0. \quad (9)$$

The function in (9) is known as the local density random walk (LDRW) model [58] with time delay t_0 . The parameter $\mu \equiv x_0/v$ (x_0 is the distance between the entry and

exit sites of the ROI) is the mean transit time needed for a microbubble to cover the distance x_0 . The parameter λ is defined as $\lambda \equiv \mu v^2/2D$, and the skewness of the curve is equal to λ^{-1} . The Peclet number (Pe) is defined as $Pe = \tau_D/\tau_c$, where τ_D is the diffusive time of contrast microbubbles (which is equal to x_0^2/D) and τ_c is the convective time, which is equal to μ . Therefore, $Pe = 2\lambda$, implying that λ can have direct physiological significance [59]. Given that this model allows for multiple passages of the microbubbles through the outlet, the average time the microbubbles stay in an ROI [known as the mean residence time (MRT) which is the first moment of $(I(t) - I_0)$ minus t_0] is larger than MTT. This property of the LDRW model should be contrasted with the gamma variate model which is the other fluid-mechanics-based model discussed in this paper. The latter is based on the assumption of unidirectional movement of the indicator particles from one mixing compartment to the next, implying $MRT = MTT$. The parameters MTT, MRT, and t_p of the LDRW model can be expressed in terms of μ and λ as follows:

$$\begin{aligned} \text{MRT} &= \mu \left(1 + \frac{1}{\lambda} \right), & \text{MTT} &= \mu, \\ t_p &= \left(\frac{\mu}{2\lambda} \right) (\sqrt{1 + 4\lambda^2} - 1). \end{aligned} \quad (10)$$

The difference between MRT and MTT is $\mu/\lambda = 2D/v^2$, implying that a large diffusion constant D leads to an increased number of microbubble passages through the outlet [60]. If the square of the blood flow velocity (v^2) is much larger than $2D$, the effects of microbubble diffusion become negligible and the value of MRT approaches the value of MTT.

Fig. 2(c) shows example curves from (9) normalized to unit peak intensity. As μ increases with λ fixed, the MTT and MRT increase and the curves become broader with slower wash-in and wash-out rates. As λ increases with μ fixed, the effects of diffusion decrease and the curves become narrower.

Sheppard and Savage [56] derived (9) using a random walk approach. The assumption behind this stochastic derivation is that the indicator particles perform a random walk motion which leads to a progressive spreading of the particles about some central abscissa. For a large number of time steps, Sheppard and Savage [56] employed the central limit theorem to obtain (9).

Like the LDRW model, the first passage time (FPT) model is also a solution of the diffusion with drift equation (10). The only difference between the two models is the boundary condition at the outlet. The FPT solution is obtained when a virtual absorbing barrier is assumed at the outlet plane—in other words, the indicator can pass only once through the boundary, whereas the LDRW solution allows multiple passages. Therefore, in the FPT model, the MRT coincides with the MTT. The solution of (10) for the FPT model [58] is given by

$$\begin{aligned} I(t) &= \text{AUC} \cdot \left(\frac{e^\lambda}{\mu} \right) \cdot \sqrt{\frac{\lambda}{2\pi}} \cdot \left(\frac{\mu}{t-t_0} \right)^{3/2} \\ &\cdot \exp \left[-\frac{1}{2} \lambda \left(\frac{\mu}{t-t_0} + \frac{t-t_0}{\mu} \right) \right] + I_0. \end{aligned} \quad (11)$$

The related parameters derived from the FPT model are given by

$$\text{MTT} = \text{MRT} = \mu, \quad t_p = \frac{\mu}{2\lambda} (\sqrt{9 + 4\lambda^2} - 3). \quad (12)$$

It can be easily seen from (10) and (12) that, in both the LDRW and FPT models, t_p is smaller than MTT. In the limit $\lambda \rightarrow \infty$ we obtain $t_p = \text{MTT}$, because the contribution of diffusion is infinitesimally small and all the particles reach the outlet at the same time μ . Often, the LDRW model is preferred over the FPT model because the FPT's assumption of an absorbing barrier at the outlet is less likely to hold than the LDRW's free boundary condition. As discussed in [59] the LDRW model gives better fits than the FPT model for small values of the parameter λ , where the effects of tracer particles diffusion are large.

The first successful application of the LDRW model to fit CEUS time-intensity curves from cardiac images has been done by Mischi *et al.* [33]. In another study, Mischi *et al.* [35] compared the performance of the LDRW model with that of the gamma variate function on time-intensity curves from both an *in vitro* study and *in vivo* cardiac images. The authors showed that both models provided accurate curve fits and blood volume estimates and they concluded that further studies are needed to carefully differentiate between the two models.

D. The Lagged Normal Function

The lagged normal function as a model for indicator dilution curves was proposed by Bassingthwaite *et al.* [61] for the case where blood from a large artery flows into a microvascular bed. The simplest lagged normal function is based on two compartments: a large vessel characterized by a Gaussian dispersion of the tracer transit times and a microvascular bed which is a homogeneous mixing compartment represented by a single exponential function. The random dispersion of the transit times of the tracer in a large vessel could be attributed to pulsatile, laminar, or turbulent flow [61]. Complete mixing of the tracer with the blood is not taking place in the large vessel, but the model assumes that the blood and the tracer have the same distribution of transit times [62]. Another interpretation put forward by Davis and Kutner [63] is that the system is composed of a mixing compartment and the Gaussian dispersion is occurring throughout the whole system.

In general, the lagged-normal functions are convolutions of a Gaussian density function with one or more exponentials. For the simplest lagged normal function with one exponential, the convolution integral is

$$I(t) = \int_{-\infty}^t f(\tau)g(t-\tau)d\tau, \quad (13)$$

where

$$\begin{aligned} f(t) &= \frac{1}{\sqrt{2\pi\sigma^2}} e^{-(t-\mu)^2/(2\sigma^2)}, \quad -\infty < t < \infty; \\ g(t) &= \lambda e^{-\lambda t}, \quad t \geq 0. \end{aligned} \quad (14)$$

The parameters μ and σ^2 are the MTT and the transit time variance of the compartment represented by the Gaussian distribution, respectively. The parameter λ is the rate constant of the mixing compartment.

By performing integration by parts and after introducing the baseline intensity offset I_0 , $I(t)$ may be expressed [62] as

$$I(t) = \frac{\text{AUC}}{2} K[1 + \text{erf}(L)] + I_0, \quad (15)$$

where

$$K = \lambda \exp\left[-\lambda t + \lambda\mu + \frac{1}{2}\lambda^2\sigma^2\right], \quad L = \frac{t - \mu - \lambda\sigma^2}{(2\sigma^2)^{1/2}},$$

with $\text{erf}(\cdot)$ being the error function.

It should be noted that the function $I(t)$ in (15) does not have a time origin, because neither the term K nor the term $[1 + \text{erf}(L)]$ become zero for any finite value of t . This model, however, has been used widely to fit indicator dilution curves, because the $[1 + \text{erf}(L)]$ term goes asymptotically to zero relatively fast. Example curves from the lagged normal function normalized to unity peak intensity are shown in Fig. 2(d). As the mixing compartment time constant λ increases for fixed σ , the rate of wash-out decreases with a small increase in the rate of wash-in, whereas as σ increases at fixed λ , the curves become more symmetric because the effects of the indicator dispersion become larger.

Davis and Kutner [63] compared the fit performances of different-order lagged normal functions (the order n is the number of exponentials convolved with the Gaussian function) on indicator dilution curves of indocyanine green in the pulmonary circulation of dogs. These authors found that the second-order lagged normal function gives slightly better fits than the first-order one. They also observed that the improvement of their fits with a third-order lagged normal function was very small.

The MTT of the first-order lagged normal function given by

$$\text{MTT} = \mu + \frac{1}{\lambda}, \quad (16)$$

which is the sum of the MTTs of the Gaussian and the exponential functions. The second moment (M_2) of the lagged normal function is given by

$$M_2 = \text{MTT}^2 + \sigma^2 + \frac{1}{\lambda^2}. \quad (17)$$

This parameter will be used for calculating the initial estimates of the fitting parameters that are provided to the nonlinear regression algorithm (Section III-B). The time to the peak intensity t_p does not exist, because the model does not have a time origin.

In the field of contrast ultrasound, the lagged normal density function has been used by Fisher *et al.* [36] to fit time-intensity curves in an investigation of myocardial and microcirculatory kinetics of BR14 (Bracco, Geneva, Switzerland). The model fitted accurately the time-intensity curves from cardiac images taken from open chest animal experiments. An empirical function which resembles the lagged normal function, the so-called Fermi-exponential function has been used by Krogias *et al.* [37] to fit CEUS time-intensity curves from cerebral perfusion imaging. The error function has been employed to extract the wash-in time of time-intensity curves in a study of blood flow changes in liver cancer during treatment [64].

III. MATERIALS AND METHODS

A. Imaging Protocol

All CEUS examinations were performed on a Philips iU22 ultrasound scanner (Philips Medical Systems, Bothell, WA). We chose to use image data from two different clinical applications: 1) The ovine corpus luteum which was surgically relocated close to the skin, without disturbing its normal function or vasculature, to allow the positioning of an ultrasound probe at an optimal and fixed position; and 2) human liver metastases. The choice of the two data sets was such as to provide one set with easy access and no motion artifacts for an easy curve analysis (corpus luteum) and one typical clinical scenario (liver metastases). The imaging parameters used for both the corpora lutea and liver metastases are shown in Table I. The nonlinear pulsing scheme employed was power modulation. In both cases, the contrast processed image was displayed side-by-side with the standard gray scale image. Image loops were acquired and saved as linearized data (following reversal of logarithmic compression and other non-linear processing). The software package QLAB (Philips Healthcare, Andover, MA) that was used for the initial analysis of the images removes the logarithmic compression used by the scanner, which is made by the same manufacturer.

The contrast injection consisted of 2.4 mL of SonoVue contrast agent (Bracco S.P.A., Milan, Italy), administered intravenously as a bolus. The 2.4 mL of contrast is within the linear range of intensity versus concentration relationship [29]. For the corpus luteum, it was injected into a catheter in the jugular vein followed by a saline flush of 10 mL that ensured that all the contrast in the line was

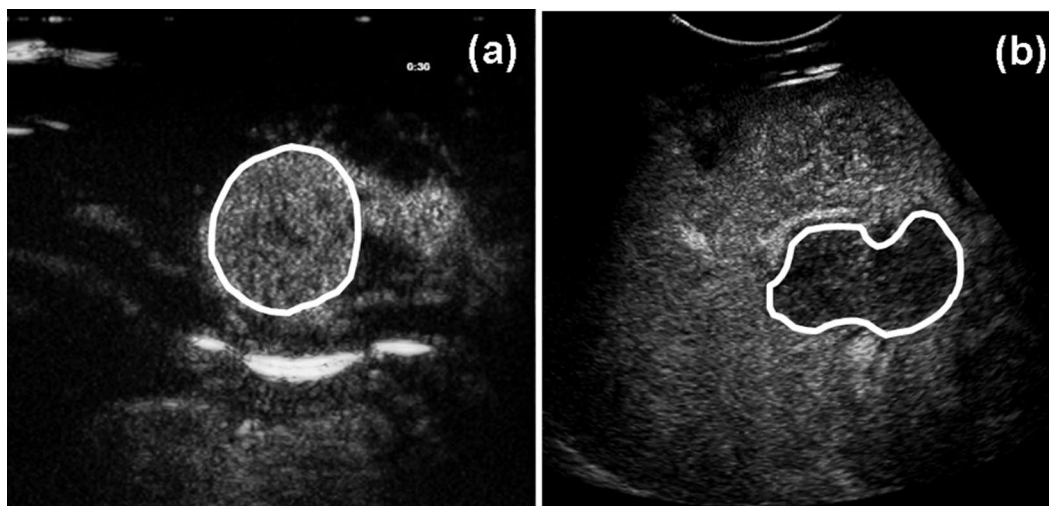


Fig. 3. Examples of contrast-enhanced ultrasound images with selected regions of interest: (a) corpus luteum at the peak enhancement and (b) liver metastasis at the late portal phase.

TABLE I. ULTRASOUND SCANNER SETTINGS FOR THE ACQUISITION OF THE LIVER METASTASIS AND THE CORPUS LUTEUM CONTRAST-ENHANCE ULTRASOUND IMAGES.

Image structure	Corpus luteum	Liver metastasis
Transducer	L9-3	C5-2
Center frequency (MHz)	3.1	1.7
Acquisition time (s)	60	120
MI (contrast)	0.05	0.06
Frame rate (Hz)	12	7-10
Dynamic range (dB)	38	38

administered to the animal. The injection to the human subjects (also 2.4 mL in volume) was followed by a saline flush of 5 mL. Patients were instructed to breathe normally (no breath holding or deep breaths) and the resulting respiratory motion in the images was removed by respiratory gating [64].

B. Image Quantification

The performance of the theoretical models discussed in Section II was evaluated by fitting them to CEUS time-intensity curves from nine image loops of liver metastases (from colorectal cancer) and ten image loops of the ovine corpus luteum. In addition to the three hemodynamic-related parameters AUC, MTT, and t_p discussed in Section II, two additional empirical parameters often used for the quantification of blood flow, namely the full-width at half-maximum (FWHM) [30] and the wash-in time (WIT) defined as the time between 5% and 95% of the peak intensity [64] were measured. The WIT and the FWHM provide alternatives to estimates for t_p and MTT, respectively, with the advantage of being independent of a time origin.

The image analysis and quantification were carried out with the commercial quantification software QLAB. The tasks included segmentation of the corpus luteum and

liver lesion (selection of an appropriate ROI for analysis) and formulation of time-intensity curves for that ROI. The measured intensity of the selected ROI for all the frames within a loop as a function of time provides the time-intensity curve for a loop. Typical images from loop captures are shown in Figs. 3(a) and 3(b) for the corpus luteum and a liver metastasis, respectively. The ROI containing the corpus luteum was selected manually based on the contrast uptake at peak intensity. The intention in drawing the ROI was to include only the microvascular network of the corpus luteum. The liver metastasis ROI was drawn based on information from the late portal phase.

A novel respiratory gating technique was utilized to minimize the effects of respiratory motion on data from the images of liver metastases [64]. A reference position of the diaphragm or any other bright interface was selected and all frames where the diaphragm deviated from that position were rejected.

To smooth the time-intensity curves and reject outliers, a standard local regression filter known as robust locally weighted scatter-plot smoothing (rloess) available in MATLAB (The MathWorks, Inc., Natick, MA) with window span five was employed before further processing. Afterwards, iterative non-linear regression fits based on the minimization of least square errors were performed on the smoothed time-intensity curves using the built-in MATLAB trust region algorithm. All models have three common fit parameters which are the AUC, t_0 and I_0 . They also have two additional parameters, except the lagged normal function which has three additional parameters. Initial estimates as well as lower and upper bounds of the fitting parameters were provided to the algorithm. For estimating the baseline intensity I_0 , an estimate of the peak intensity I_p is first needed. The latter is obtained by averaging the values of I in the range where the intensity is greater than 90% of the maximum intensity in the wash-in and wash-out parts of the curve.

For the initial estimate of I_0 , the latest point in time in the wash-in part of the curve where the intensity is less than 2% of the estimate of I_p is first found. Then, all the intensity values until that time are averaged to obtain the initial estimate for I_0 . The lower bound for I_0 is set to zero and the upper bound is set to 1.2 times the initial estimate of I_0 . The last point in time during wash-in where the intensity is less than or equal to the estimate for I_0 is the initial estimate for the time origin t_0 which is set to zero. The upper bound of t_0 is set to 10 s and the lower bound is set to -10 s for all models except for the LDRW and FPT, where the upper bound is set to zero to avoid the root of negative numbers [see (9) and (11)]. If the algorithm hits a bound, then both the estimate and the bounds are shifted by 1 s for all models (because all models must be fitted to the same data) and the new estimate of t_0 is set to zero. This procedure is repeated until the fitting algorithm does not hit a bound for any of the models. All the data points that correspond to values of t smaller than the initial estimate of the time origin are not included in the curve-fitting process. The initial estimate of AUC is obtained from a numerical integration of the time-intensity curve with the trapezoidal rule. The width of each trapezoid is the time between consecutive frames. The initial estimates of the other parameters are calculated in terms of t_p , and the first and second moments of the time-intensity curves. The estimate for t_p is the mean of all values of t in the wash-in and wash-out parts of the time-intensity curve where I is larger than 90% of the peak intensity. The initial estimates of the parameters μ and σ of the lognormal model are obtained by solving (3). Similarly, the initial estimates of parameters α and β of the gamma variate model are obtained by solving (7). The estimates for the parameters μ and λ of the LDRW and FPT models are obtained from the solution of a system of two equations for the first and second moments of the time-intensity curve which can be expressed in terms of μ and λ [65]. For the lagged normal function, the initial estimate of λ is obtained from a single exponential fit (which reduces to a linear fit after a logarithmic transformation) to the wash-out tails of time-intensity curves. Subsequently, the estimates of μ and σ^2 are obtained from (16) and (17), respectively. The convergence time of the algorithm varied from one to three seconds with small differences among the various models, on a Windows-based workstation Intel Core Duo 2.4 GHz with 4 GB of RAM.

In certain cases, the wash-out parts of time-intensity curves were affected by the recirculation of the contrast microbubbles. However, the models employed for this study are not well suited for fitting the second circulation, at least without any further modifications. Therefore, to isolate the primary pass of the indicator, the fitting window was truncated to the point in the wash-out tail where the value of the intensity is 25% and 5% of the maximum intensity value for the liver metastasis and corpus luteum data sets, respectively. The choice of truncation was empirical and based on the data available.

For a quantitative assessment of the models' performances, two parameters were calculated, namely the coefficient of determination (R^2) and the root mean square error (RMSE). The coefficient of determination is the fraction of variation in the data that is accounted for by the regression model, and the RMSE is the average distance of the data points from the fitted line. For a comparison of the models' performance, the average values of R^2 and their standard deviations were measured for all liver metastasis and corpus luteum data separately. Unlike R^2 , the RMSE values do not have an upper bound. Therefore, to compare the RMSE values produced by the different models, we implemented the following normalization procedure: the value of RMSE produced by each model on each time-intensity curve was normalized with respect to the average RMSE produced by all models. Subsequently, the average values of the normalized RMSE and their standard deviations were calculated separately for all liver metastasis and corpus luteum data sets. The same procedure for parameter normalization and averaging was repeated for the hemodynamic-related parameters AUC, MTT, FWHM, t_p , and WIT.

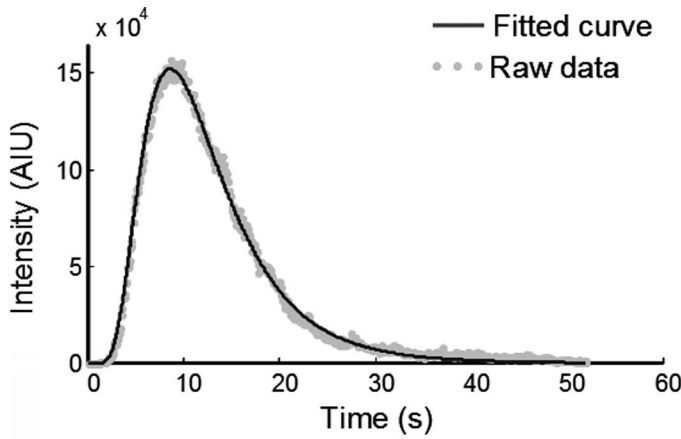
The LDRW model is the only one that allows for a clear distinction between MTT and MRT [see (10)], because it allows multiple passages of the microbubbles through an outlet. The difference between the values of these two parameters is quantified by the parameter d , which is defined as follows:

$$d \equiv \frac{\text{MRT} - \text{MTT}}{\text{MRT}} = \frac{1}{1 + \lambda}. \quad (18)$$

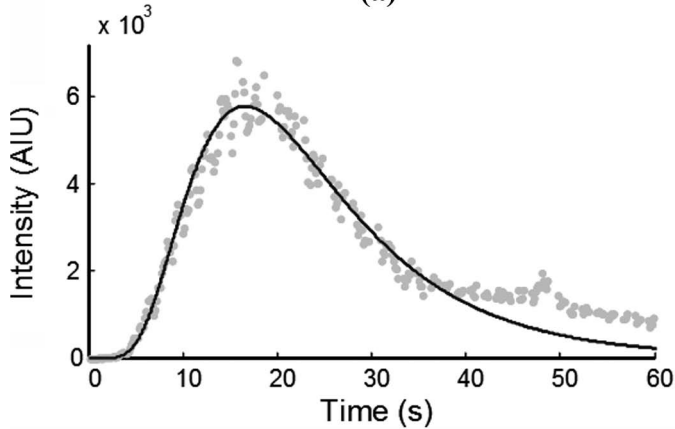
IV. RESULTS

Figs. 4(a) and 4(b) show typical examples of time-intensity curves from a corpus luteum and a liver metastasis, respectively, together with the fitting functions of the lognormal model. The fitting ranges include all the data from the estimated arrival times until $t = 19$ s and $t = 21$ s for the corpus luteum and liver metastasis data, respectively. The fit qualities of the lognormal model on the two time-intensity curves are $R^2 = 1.00$, RMSE = 2788 for the corpus luteum, and $R^2 = 0.97$, RMSE = 358 for the liver lesion. The values of R^2 imply that the model fitted both time-intensity curves well with the fit quality on the corpus luteum data being slightly better than on the liver metastasis data. The fit on the corpus luteum data produced a larger RMSE, because the larger intensity values (because a different probe and frequency were used) in this data set result in a larger absolute value of RMSE.

Fig. 5(a) shows the fitting functions produced by all models on a corpus luteum time-intensity curve and Fig. 5(b) is a magnification of Fig. 5(a) near the time origin. As shown in these figures, the lognormal function and the two models based on diffusion with drift (LDRW and FPT) fitted the various parts of the time-intensity curve well. In addition, the LDRW and FPT models produced



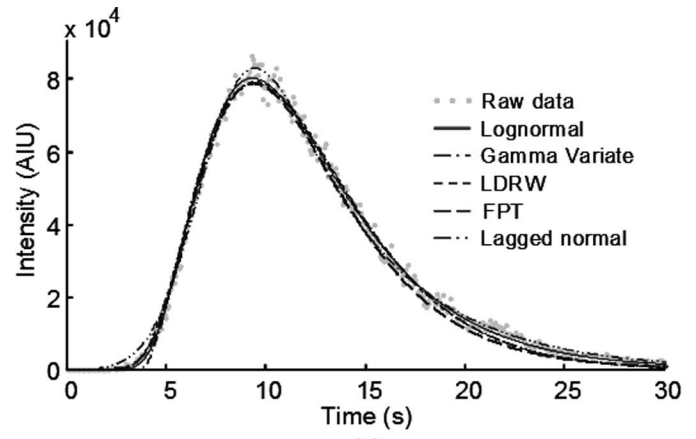
(a)



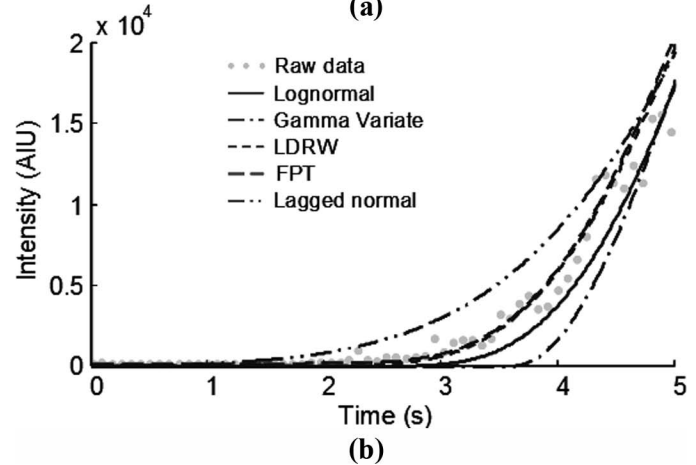
(b)

Fig. 4. Examples of fitted curves [arbitrary intensity units (AIU)] with the lognormal function on (a) a corpus luteum and (b) liver metastasis time-intensity curves.

curves that are very close to each other. Near the time origin, the gamma variate function produced a curve which is steeper than the data and the lagged normal function produced a curve which lags behind the data. The lagged normal function is also slightly slow in the wash-out part of the curve. The same procedure was repeated on a liver metastasis time-intensity curve and the results are shown in Figs. 6(a) and (b). It can be seen from these figures that the fits produced by all models follow similar trends as in Figs. 5(a) and (b).



(a)



(b)

Fig. 5. (a) An ovine corpus luteum time-intensity curve fitted with five models: the lognormal, the gamma variate, the local density random walk (LDRW), the first passage time (FPT), and the lagged normal; (b) a magnification of (a) near the time origin (the lines for LDRW and FPT are very close to each other).

The average values of R^2 and RMSE (and their standard deviations) for the corpus luteum and the liver metastasis data sets are presented in Tables II and III, respectively. Observing the values of the fit quality parameters, it may be deduced that the various models have comparable fit performances on both data sets. The lower fit qualities of the gamma variate and the lagged normal functions in a small region near the time origin have a small impact on the overall fit performances of these models, because the width of this region is small.

TABLE II. THE AVERAGE R^2 AND ROOT MEAN SQUARE ERROR (RMSE) EXTRACTED FROM CURVE-FITS WITH ALL THE MODELS ON THE CORPUS LUTEUM DATA.

	Lognormal	Gamma variate	LDRW	FPT	Lagged normal
R^2	0.96 ± 0.02	0.96 ± 0.02	0.96 ± 0.02	0.96 ± 0.02	0.96 ± 0.02
RMSE	1.01 ± 0.09	1.04 ± 0.08	0.98 ± 0.04	0.97 ± 0.04	1.00 ± 0.11

TABLE III. THE AVERAGE R^2 AND ROOT MEAN SQUARE ERROR (RMSE) EXTRACTED FROM CURVE-FITS WITH ALL THE MODELS ON THE LIVER METASTASIS DATA.

	Lognormal	Gamma variate	LDRW	FPT	Lagged normal
R^2	0.92 ± 0.06	0.91 ± 0.06	0.92 ± 0.06	0.92 ± 0.06	0.92 ± 0.06
RMSE	1.00 ± 0.02	1.08 ± 0.15	1.00 ± 0.02	0.98 ± 0.03	0.93 ± 0.15

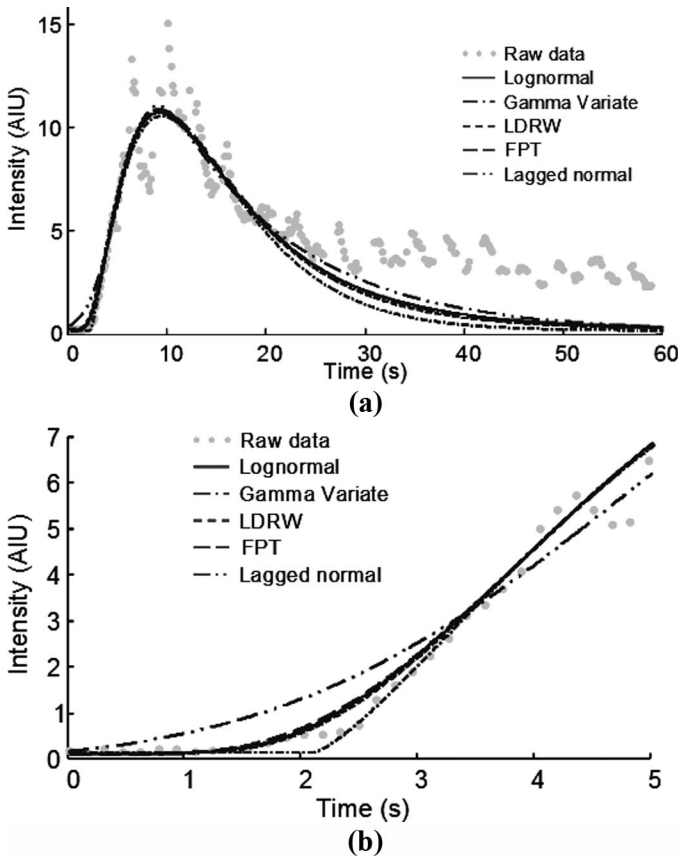


Fig. 6. (a) A liver metastasis time-intensity curve fitted with five models: the lognormal, the gamma variate, the local density random walk (LDRW), the first passage time (FPT), and the lagged normal with a single exponential, (b) a magnification of (a) near the time origin (the lines for LDRW and FPT are very close to each other).

The results for the average values of the normalized hemodynamic-related parameters together with their standard deviations for both the corpus luteum and the liver metastasis data sets are shown in Tables IV and V, respectively. The trends in the behaviors of the models on both data sets are similar. In general, a good agreement is observed between the values of the hemodynamic-related parameters extracted from curve fittings with the lognormal function and the FPT model, with the parameter t_p being the only exception. The values of AUC, MTT, and t_p extracted from fits with the gamma variate function are smaller than those produced by the other models. Both the LDRW and the FPT models produced values of t_p that are larger than the values produced by the other models. Also, the average values of MTT extracted from the LDRW model are smaller than the average values of this parameter extracted from the lognormal, the FPT and the lagged normal models. The values of the parameter d , which quantifies the difference between the parameters MRT and MTT for the LDRW model, are 0.30 ± 0.15 and 0.15 ± 0.08 for the liver metastasis and corpus luteum data sets, respectively. The results for MRT from the LDRW model and MTT from all other models (MRT = MTT for all models except the LDRW) are shown in Table VI. It is observed that the average value of MRT from the LDRW agrees within one standard deviation with the average values of MTT extracted from the other models. The WIT has a smaller variation among models as compared with AUC, MTT, and t_p , whereas the FWHM is the most stable parameter, with the smallest dependence on the choice of the regression model, because it does not depend on the fit quality near the time origin.

TABLE IV. NORMALIZED HEMODYNAMIC PARAMETERS¹ EXTRACTED FROM FITS ON THE CORPUS LUTEUM DATA SET WITH ALL MODELS.

	Lognormal	Gamma variate	LDRW	FPT	Lagged normal
AUC	1.01 ± 0.04	0.95 ± 0.04	0.96 ± 0.02	0.97 ± 0.02	1.11 ± 0.05
MTT	1.09 ± 0.03	0.85 ± 0.02	0.94 ± 0.11	1.13 ± 0.02	0.99 ± 0.14
FWHM	1.01 ± 0.03	1.01 ± 0.03	1.00 ± 0.02	1.00 ± 0.02	0.99 ± 0.04
t_p	1.05 ± 0.10	0.85 ± 0.03	1.13 ± 0.04	1.17 ± 0.04	—
WIT	0.97 ± 0.05	0.97 ± 0.02	0.98 ± 0.02	0.99 ± 0.02	1.09 ± 0.04

¹AUC = area under the time-intensity curve; MTT = mean transit time; FWHM = full-width at half-maximum; t_p = time to the peak intensity; WIT = wash-in time.

TABLE V. NORMALIZED HEMODYNAMIC PARAMETERS¹ EXTRACTED FROM FITS ON THE LIVER METASTASIS DATA SET WITH ALL MODELS.

	Lognormal	Gamma variate	LDRW	FPT	Lagged normal
AUC	1.00 ± 0.02	0.87 ± 0.07	0.95 ± 0.02	1.05 ± 0.10	1.12 ± 0.10
MTT	1.07 ± 0.13	0.77 ± 0.13	0.75 ± 0.21	1.17 ± 0.15	1.00 ± 0.20
FWHM	1.00 ± 0.01	0.98 ± 0.03	1.00 ± 0.01	1.00 ± 0.01	1.03 ± 0.05
t_p	1.04 ± 0.06	0.90 ± 0.04	1.10 ± 0.05	1.15 ± 0.04	—
WIT	1.01 ± 0.03	0.97 ± 0.06	1.00 ± 0.03	1.02 ± 0.04	0.99 ± 0.07

¹AUC = area under the time-intensity curve; MTT = mean transit time; FWHM = full-width at half-maximum; t_p = time to the peak intensity; WIT = wash-in time.

TABLE VI. NORMALIZED VALUES OF MEAN TRANSIT TIME (MTT) EXTRACTED FROM FITS WITH DIFFERENT MODELS¹ (EXCEPT LDRW) AND THE VALUES OF MEAN RESIDENCE TIME (MRT) EXTRACTED FROM FITS WITH THE LDRW MODEL.¹

	Lognormal MTT	Gamma variate MTT	LDRW MRT	FPT MTT	Lagged normal MTT
Liver metastasis	1.02 ± 0.13	0.74 ± 0.16	0.95 ± 0.18	1.11 ± 0.13	0.95 ± 0.19
Corpus luteum	1.06 ± 0.03	0.82 ± 0.03	1.06 ± 0.08	1.10 ± 0.03	0.96 ± 0.12

¹LDRW = local density random walk; FPT = first passage time.

V. DISCUSSION

Mathematical models can be employed to fit indicator dilution curves to filter out the noise and isolate the primary pass of the indicator. In addition, a model that fits the data well may help to interpret the primary pass, because it describes the functional relationship among the variables of the system under study. Contrast ultrasound image data from both the macro- and microcirculation can be modeled with indicator dilution theory. The objective of utilizing such models is the estimation of hemodynamic-related parameters such as the AUC, MTT, FWHM, t_p , and WIT, which in turn may lead to quantification of microcirculation in various clinical scenarios.

We have presented the physical and physiological basis of different indicator dilution models namely the lognormal function, the gamma variate function, the diffusion with drift models (LDRW and FPT), and the lagged normal function. We evaluated the models' performances on CEUS image data from human liver metastases and exposed ovine corpora lutea. Despite the comparable values of fit, quality parameters (R^2 and RMSE) produced by the various models on both data sets, there are differences between the fit performances of certain models near the time origin and the wash-out tail, implying that the overall fit quality parameters are not always adequate measures of a model's performance. The lognormal function and the diffusion with drift models (LDRW and FPT) are the most accurate models, because they fitted well the time-intensity curves from both the liver metastasis and the corpus luteum for the entire fitting range.

As shown in the analytical work of Qian and Bassingthwaite [49], the lognormal function is an appropriate indicator dilution model for microvascular networks with a large number of generations. The gamma variate function, which is based on unidirectional motion of the indicator particles from one mixing chamber to the next [35], does not properly model the indicator diffusion, which would otherwise smooth sharp changes in the gradient. As a consequence, this model tends to overestimate the value of the time origin t_0 and underestimate the values of AUC, MTT, and t_p . The LDRW and FPT models work well for microvascular networks with a diffusive architecture, because they explicitly take diffusion into account. In addition, the LDRW is the only model that allows for a distinction between MRT and MTT. The values of MTT estimated by this model are significantly smaller than the estimated values of MRT. This result is encountered when

the LDRW model is used to fit skewed curves with finite values of the parameter λ , where the effects of microbubble diffusion are non-negligible. The LDRW model also produced values of MTT which are, on average, smaller than the values of MTT produced by the lognormal, the FPT, and the lagged normal models. The average values of MRT extracted from fits with the LDRW model agree within one standard deviation with the values of MTT extracted from the other models, the gamma variate function being the only exception. A comparison of volume and flow rate estimates in phantom experiments based on hemodynamic-related parameters extracted from curve fits with the lognormal and the diffusion with drift models may give further insight into the specific properties of these models. The lagged normal function produces estimates of AUC that are larger than the estimates produced by the other models, especially when it fits very skewed time-intensity curves. This is attributed to the fact that the wash-in part of this model is dominated by a term which does not have a time origin and the wash-out part is dominated by a single exponential term which decays slowly. The latter is reminiscent of earlier criticism on modeling the wash-out parts of indicator dilution curves with a single exponential function as suggested by Hamilton *et al.* almost a century ago [16]. The empirical parameter FWHM has the smallest variation among models, because it does not depend on the fit quality near the time origin. Therefore, it may be a useful parameter to monitor during treatment in oncology and other clinical scenarios.

The parameters MTT, FWHM, t_p , and WIT are accurately measured in CEUS, because they are rather independent of ultrasound scanner settings (they are time measurements). The parameter AUC is more sensitive on imaging parameters (depth, attenuation, and frequency) and thus it may not be as reproducible as the time parameters. The dependence of the parameters on the fit quality near the time origin can be reduced with the choice of an appropriate model as discussed earlier. For the parameters that depend on the wash-out of the indicator (AUC, MTT, and FWHM), it is important to eliminate possible recirculation effects by curve-fitting the data in an appropriate fitting interval.

Quantification of blood flow and blood volume at the microcirculation level with the aid of indicator dilution models will help the on-going research in therapy monitoring in various oncology applications. Another promising application of mathematical modeling of the microcirculation is parametric imaging, which is the formation of a

functional image from new parameters (often a combination of two or more) extracted from the mathematical models fitted on perfusion data at the pixel level or in small groups of pixels.

VI. CONCLUSIONS

All major indicator dilution models, namely the lognormal function, the gamma variate function, the LDRW and FPT models, and the lagged normal function, have been discussed in detail and compared with one another. The validity of these models for use with CEUS was investigated with a large number of image loops from an animal model of microflow in the ovaries and from human liver metastases. From our analysis, we conclude that the models with the best performances are the lognormal function and the diffusion with drift models, because their physiological and physical basis takes into consideration the architecture of microvascular networks. With the choice of an appropriate model, various hemodynamic-related parameters (AUC, MTT, FWHM, t_p , and WIT) can be measured accurately. An application-specific model may be selected after analysis of more *in vitro* and *in vivo* data.

ACKNOWLEDGMENTS

We thank Dr. K. Kyriakopoulou for her help in acquiring the liver metastasis image loops. We also thank the two anonymous reviewers for valuable comments and suggestions.

REFERENCES

- [1] D. Cosgrove, "Ultrasound contrast agents: An overview," *Eur. J. Radiol.*, vol. 60, pp. 324–330, Dec. 2006.
- [2] C. J. Harvey, J. M. Pilcher, R. J. Eckersley, M. J. K. Blomley, and D. O. Cosgrove, "Advances in ultrasound," *Clin. Radiol.*, vol. 57, no. 3, pp. 157–177, Mar. 2002.
- [3] M. Averkiou, J. Powers, D. Skyba, M. Bruce, and S. Jensen, "Ultrasound contrast imaging research," *Ultrasound Q.*, vol. 19, no. 1, pp. 27–37, 2003.
- [4] P. N. Burns, D. Hope Simpson, and M. A. Averkiou, "Nonlinear imaging," *Ultrasound Med. Biol.*, vol. 26, suppl.1, pp. S19–S22, May 2000.
- [5] G. A. Schwartz and M. A. Averkiou, "Future directions—New developments in ultrasound," in *Imaging in Oncological Urology*, J. de la Rosette, M. Harisinghani, M. Manyak, and H. Wijkstra, Eds., London, UK: Springer-Verlag, 2009, pp. 373–379.
- [6] E. Leen, P. Ceccotti, S. J. Moug, P. Glen, J. MacQuarrie, W. J. Angerson, T. Albrecht, J. Hohmann, A. Oldenburg, J. P. Ritz, and P. G. Horgan, "Potential value of contrast-enhanced intraoperative ultrasonography during partial hepatectomy for metastases: An essential investigation before resection?" *Ann. Surg.*, vol. 243, no. 2, pp. 236–240, Feb., 2006.
- [7] M. J. Blomley, T. Albrecht, D. O. Cosgrove, V. Jayaram, R. J. Eckersley, N. Patel, S. Taylor-Robinson, A. Bauer, and R. Schlieff, "Liver vascular transit time analyzed with dynamic hepatic venography with bolus injections of an US contrast agent: Early experience in seven patients with metastases," *Radiology*, vol. 209, no. 3, pp. 862–866, Dec. 1998.
- [8] E. J. Halpern, L. Verkh, F. Forsberg, L. G. Gomella, R. F. Mattrey, and B. B. Goldberg, "Initial experience with contrast-enhanced sonography of the prostate," *AJR Am. J. Roentgenol.*, vol. 174, no. 6, pp. 1575–1580, Jun. 2000.
- [9] R. J. Eckersley, J. P. Michiel Sedelaar, M. J. K. Blomley, H. Wijkstra, N. M. deSouza, D. O. Cosgrove, and J. J. M. C. H. de la Rosette, "Quantitative microbubble enhanced transrectal ultrasound as a tool for monitoring hormonal treatment of prostate carcinoma," *Prostate*, vol. 51, no. 4, pp. 256–267, Jun. 2002.
- [10] J. M. Correas, M. Claudon, F. Tranquart, and A. O. Helenon, "The kidney: Imaging with microbubble contrast agents," *Ultrasound Q.*, vol. 22, no. 1, pp. 53–66, Mar. 2006.
- [11] G. Rizzatto, A. Martegani, R. Chersevani, D. Macorig, M. Vrtovec, L. Aiari, and L. Tufarulo, "Importance of staging of breast cancer and role of contrast ultrasound," *Eur. Radiol.*, vol. 11, suppl. 3, pp. E47–E52, Dec. 2001.
- [12] K. Wei, A. R. Jayaweera, S. Firoozan, A. Linka, D. M. Skypa, and S. Kaul, "Quantification of myocardial blood flow with ultrasound-induced destruction of microbubbles administered as a constant venous infusion," *Circulation*, vol. 97, no. 5, pp. 473–483, Feb. 1998.
- [13] G. N. Stewart, "Researches on the circulation time and on the influences which affect it. IV. The output of the heart," *J. Physiol.*, vol. 22, pp. 159–183, 1897.
- [14] V. Henriques, "Über die Verteilung des Blutes vom linken Herzen zwischen dem Herzen und dem übrigen Organismus," *Biochem. Z.*, vol. 56, pp. 230–248, 1913.
- [15] W. F. Hamilton, J. W. Moore, J. M. Kinsman, and R. G. Spurling, "Simultaneous determination of the pulmonary and systemic circulation times in man and of a figure related to cardiac output," *Am. J. Physiol.*, vol. 84, pp. 338–344, Mar. 1928.
- [16] W. F. Hamilton, J. W. Moore, J. M. Kinsman, and R. G. Spurling, "Studies of the circulation: VI. Further analysis of the injection method and of changes of hemodynamic under physiological conditions," *Am. J. Physiol.*, vol. 99, no. 3, pp. 534–551, 1932.
- [17] J. L. Stephenson, "Theory of the measurement of blood flow by the dilution of an indicator," *Bull. Math. Biophys.*, vol. 10, no. 3, pp. 117–121, Sep. 1948.
- [18] C. W. Sheppard, "Mathematical considerations of indicator dilution techniques," *Minn. Med.*, vol. 37, no. 2, pp. 93–104, Feb. 1954.
- [19] P. Meier and K. L. Zierler, "On the theory of indicator-dilution method for measurement of blood flow and volume," *J. Appl. Physiol.*, vol. 6, no. 12, pp. 731–744, Jun. 1954.
- [20] P. Dow, "Estimations of cardiac output and central blood volume by dye dilution," *Physiol. Rev.*, vol. 36, no. 1, pp. 77–102, 1956.
- [21] C. W. Sheppard, *Basic Principles of the Tracer Method: Introduction to Mathematical Tracer Kinetics*. New York, NY: Wiley, 1962.
- [22] K. L. Zierler, "Theoretical basis of indicator-dilution methods for measuring flow and volume," *Circ. Res.*, vol. 10, pp. 393–407, Mar. 1962.
- [23] V. Mor-Avi, D. David, S. Akselrod, Y. Bitton, and I. Choshniak, "Myocardial regional blood flow: Quantitative measurement by computer analysis of contrast enhanced echocardiographic images," *Ultrasound Med. Biol.*, vol. 19, no. 8, pp. 619–633, 1993.
- [24] W. H. Pritchard, W. J. MacIntyre, and T. W. Moir, "The determination of cardiac output by the dilution method without arterial sampling: II Validation of precordial recording," *Circulation*, vol. 18, no. 6, pp. 1147–1154, Dec. 1958.
- [25] P. S. Tofts, "Modeling tracer kinetics in dynamic Gd-DTPA MR imaging," *J. Magn. Reson. Imag.*, vol. 7, no. 1, pp. 91–101, Jan.-Feb., 1997.
- [26] K. A. Miles, M. Hayball, and A. K. Dixon, "Colour perfusion imaging: A new application of computed tomography," *Lancet*, vol. 337, pp. 643–645, Mar. 1991.
- [27] K. Tiemann, T. Schlosser, C. Pohl, D. Bimmel, G. Wietasch, A. Hoeft, J. Likungu, C. Vahlhaus, S. Kuntz, N. C. Nanda, H. Becher, and B. Lüderitz, "Are microbubbles free flowing tracers through the myocardium? Comparison of indicator-dilution curves obtained from dye dilution and echo contrast using harmonic power Doppler imaging," *Echocardiography*, vol. 17, no. 1, pp. 17–27, Jan. 2000.
- [28] T. Schlosser, C. Pohl, S. Kuntz-Hehner, H. Omran, H. Becher, and K. Tiemann, "Echoscintigraphy: A new imaging modality for the reduction of color blooming and acoustic shadowing in contrast sonography," *Ultrasound Med. Biol.*, vol. 29, no. 7, pp. 985–991, Jul. 2003.
- [29] M. Lampaskis and M. A. Averkiou, "Investigation of the relationship of non-linear backscattered ultrasound intensity with microbubble concentration at low MI," *Ultrasound Med. Biol.*, vol. 36, no. 2, pp. 306–312, Feb. 2010.
- [30] N. Lassau, L. Chami, B. Benatsou, P. Peronneau, and A. Roche, "Dynamic contrast-enhanced ultrasonography (DCE-US) with

- quantification of tumor perfusion: A new diagnostic tool to evaluate the early effects of antiangiogenic treatment," *Eur. Radiol.*, vol. 17, suppl. 6, pp. F89-F98, Dec. 2007.
- [31] G. Renault, F. Tranquart, V. Perlbarg, A. Bleuzen, A. Herment, and F. Frouin, "A posteriori respiratory gating in contrast ultrasound for assessment of hepatic perfusion," *Phys. Med. Biol.*, vol. 50, pp. 4465-4480, Jun. 2005.
- [32] G. J. Lueck, T. K. Kim, P. N. Burns, and A. L. Martel, "Hepatic perfusion imaging using factor analysis of contrast enhanced ultrasound," *IEEE Trans. Med. Imaging*, vol. 27, no. 10, pp. 1449-1457, Oct. 2008.
- [33] M. Mischi, T. Kalker, and E. Korsten, "Videodensitometric methods for cardiac output measurements," *EURASIP J. Appl. Signal Process.*, vol. 5, pp. 479-489, Jan. 2003.
- [34] G. H. Wasmeier, W.-H. Zimmermann, N. Schineis, I. Melnychenko, J.-U. Voigt, T. Eschenhagen, F. A. Flachskampf, W. G. Daniel, and U. Nixdorff, "Real-time myocardial contrast echocardiography for assessing perfusion and function in healthy and infarcted wistar rats," *Ultrasound Med. Biol.*, vol. 34, no. 1, pp. 47-55, Jan. 2008.
- [35] M. Mischi, J. A. der Boer, and H. H. M. Korsten, "On the physical and stochastic representation of an indicator dilution curve as a gamma variate," *Physiol. Meas.*, vol. 29, no. 3, pp. 281-294, 2008.
- [36] N. G. Fisher, J. P. Christiansen, H. Leong-Poi, A. R. Jayaweera, J. R. Lindner, and S. Kaul, "Myocardial and microcirculatory kinetics of BR14, a novel third-generation intravenous ultrasound contrast agent," *J. Am. Coll. Radiol.*, vol. 39, no. 3, pp. 530-537, Feb. 2002.
- [37] C. Krogias, T. Postert, S. Meves, W. Wilkening, H. Przuntek, and J. Eyding, "Semi-quantitative analysis of ultrasonic cerebral perfusion imaging," *Ultrasound Med. Biol.*, vol. 31, no. 8, pp. 1007-1012, Aug. 2005.
- [38] J. M. Thijssen and C. L. de Korte, "Modeling ultrasound contrast measurement of blood flow and perfusion in biological tissue," *Ultrasound Med. Biol.*, vol. 31, no. 2, pp. 279-285, Feb. 2005.
- [39] P.-C. Li and M.-J. Yang, "Transfer function analysis of ultrasonic time-intensity measurements," *Ultrasound Med. Biol.*, vol. 29, no. 10, pp. 1493-1500, Oct. 2003.
- [40] L. E. Derchi, C. Martinoli, F. Pretolesi, G. Crespi, and D. Buccinardi, "Quantitative analysis of contrast enhancement," *Eur. Radiol.*, vol. 9, suppl. 3, pp. S372-S376, 1999.
- [41] M. Arditi, P. J. A. Frinking, X. Zhou, and N. G. Rognin, "A new formalism for the quantification of tissue perfusion by the destruction-replenishment method in contrast ultrasound imaging," *IEEE Trans. Ultrason. Ferroelectr. Freq. Control*, vol. 53, no. 6, pp. 1118-1129, Jun. 2006.
- [42] A. L. Koch, "The logarithm in biology: I. Mechanisms generating the log-normal distribution," *J. Theor. Biol.*, vol. 12, no. 2, pp. 276-290, Nov. 1966.
- [43] A. L. Koch, "The logarithm in biology: II. Distributions simulation the log-normal," *J. Theor. Biol.*, vol. 23, no. 2, pp. 251-268, May. 1969.
- [44] E. Limpert, W. A. Stahel, and M. Abbt, "Log-normal distributions across the sciences: Keys and clues," *Bioscience*, vol. 51, no. 5, pp. 341-352, May 2001.
- [45] R. W. Stow and P. S. Hetzel, "An empirical formula for indicator-dilution curves as obtained in human beings," *J. Appl. Physiol.*, vol. 7, no. 2, pp. 161-167, Sep. 1954.
- [46] M. E. Wise, "The geometry of log-normal and related distributions and an application to tracer-dilution curves," *Stat. Neerl.*, vol. 20, no. 1, pp. 119-142, 1966.
- [47] R. A. F. Linton, N. W. F. Linton, and D. M. Band, "A new method of analyzing indicator dilution curves," *Cardiovasc. Res.*, vol. 30, no. 6, pp. 930-938, Dec. 1995.
- [48] D. M. Band, R. A. F. Linton, T. K. O'Brien, M. M. Jonas, and N. W. F. Linton, "The shape of indicator dilution curves used for cardiac output measurement in man," *J. Physiol.*, vol. 498, no. 1, pp. 225-229, Jan. 1997.
- [49] H. Qian and J. B. Bassingthwaighe, "A class of flow bifurcation models with lognormal distribution and fractal dispersion," *J. Theor. Biol.*, vol. 205, no. 2, pp. 261-268, Jul. 2000.
- [50] J. H. Van Beek, S. A. Roger, and J. B. Bassingthwaighe, "Regional myocardial flow heterogeneity explained with fractal networks," *Am. J. Physiol. Heart Circ. Physiol.*, vol. 257, no. 5, pp. H1670-H1680, 1989.
- [51] E. J. Schlossmacher, H. Weinstein, S. Lochaya, and A. B. Shaffer, "Perfect mixers in series model for fitting venoarterial indicator-dilution curves," *J. Appl. Physiol.*, vol. 22, no. 2, pp. 327-332, Feb. 1967.
- [52] R. Davenport, "The derivation of the gamma-variate relationship for tracer dilution curves," *J. Nucl. Med.*, vol. 24, no. 10, pp. 945-948, 1983.
- [53] H. K. Thompson, C. F. Starmer, R. E. Whalen, and H. D. McIntosh, "Indicator transit time considered as a gamma variate," *Circ. Res.*, vol. 14, pp. 501-515, Jun. 1964.
- [54] X. Li, J. Tian, and R. K. Millard, "Erroneous and inappropriate use of gamma fits to tracer-dilution curves in magnetic resonance imaging and nuclear medicine," *Magn. Reson. Imag.*, vol. 21, no. 9, pp. 1095-1096, Nov. 2003.
- [55] E. V. Newman, M. Merrell, A. Genecin, C. Monge, W. R. Milnor, and W. P. McKeever, "The dye dilution method for describing the central circulation. An analysis of factors shaping the time-concentration curves," *Circulation*, vol. 4, no. 5, pp. 735-746, 1951.
- [56] C. W. Sheppard and L. J. Savage, "The random walk problem in relation to the physiology of circulatory mixing," *Phys. Rev.*, vol. 83, pp. 489-490, Jul.-Sep. 1951.
- [57] K. H. Norwich and S. Zerlin, "The dispersion of indicator in the cardio-pulmonary system," *Bull. Math. Biophys.*, vol. 32, no. 1, pp. 25-43, Mar. 1970.
- [58] M. E. Wise, "Tracer dilution curves in cardiology and random walk and lognormal distributions," *Acta Physiol. Pharmacol. Neerl.*, vol. 14, no. 2, pp. 175-204, 1966.
- [59] J. M. Bogaard, S. J. Smith, A. Versprille, M. E. Wise, and F. Hagemeyer, "Physiological interpretation of the skewness of indicator-dilution curves; Theoretical considerations and a practical application," *Basic Res. Cardiol.*, vol. 79, no. 4, pp. 479-493, Jul. 1984.
- [60] M. Mischi, T. A. Kalker, and E. H. Korsten, "Contrast echocardiography for pulmonary blood volume quantification," *IEEE Trans. Ultrason. Ferroelectr. Freq. Control*, vol. 51, no. 9, pp. 1137-1147, Sep. 2004.
- [61] J. B. Bassingthwaighe, F. H. Ackerman, and E. H. Wood, "Applications of the lagged normal density function curve as a model for arterial dilution curves," *Circ. Res.*, vol. 18, no. 4, pp. 398-415, 1966.
- [62] N. L. Eigler, J. M. Pfaff, A. Zeiher, J. S. Whiting, and J. S. Forrester, "Digital angiographic impulse response analysis of regional myocardial perfusion: Linearity, reproducibility, accuracy, and comparison with conventional indicator dilution curve parameters in phantom and canine models," *Circ. Res.*, vol. 64, no. 5, pp. 853-866, May 1989.
- [63] G. C. Davis and M. H. Kutner, "The lagged normal family of probability density functions applied to indicator-dilution curves," *Biometrics*, vol. 32, no. 3, pp. 669-675, Sep. 1976.
- [64] M. Averkiou, M. Lampaskis, K. Kyriakopoulou, D. Skarlos, G. Klouvas, C. Strouthos, and E. Leen, "Quantification of tumor microvasculature with respiratory gated contrast enhanced ultrasound for monitoring therapy," *Ultrasound Med. Biol.*, vol. 36, no. 1, pp. 68-77, Jan. 2010.
- [65] M. Mischi, A. C. C. M. Kalker, and H. H. M. Korsten, "Moment method for the local density random walk model interpolation of ultrasound contrast agent dilution curves," in *Proc. 17th Int. EURASIP Conf. BIOSIGNAL 2004*, Brno, Czech Republic, pp. 33-35.



Costas Strouthos received a B.Sc. (Hons.) degree in physics from Imperial College London in 1989, the Certificate of Advanced Study in Mathematics from Cambridge University in 1991, and the M.S. and Ph. D. degrees in physics from the University of Illinois at Urbana-Champaign in 1998 and 1999, respectively.

He worked as a Research Officer in physics at Swansea University from 1999 to 2002, as a Research Associate in physics at Duke University from 2003 to 2004, as a Research Fellow at the Harvard-MIT Martinos Center for Biomedical Imaging from 2005 to 2006, and as a Scientific Collaborator at the Swiss Federal Institute of Technology Lausanne from 2006 to 2007. Since 2007 he has been a Special Scientist in the Department of Mechanical and Manufacturing Engineering at the University of Cyprus. His main research interests are in computational physics and biomedical modeling and computation.

Dr. Strouthos has (co)-authored 44 papers in peer-reviewed journals and conference proceedings.



Marios Lampaskis received an M.Eng. degree in automatic control and systems engineering in 2004 with a thesis in heart rate control of subjects under physical stress. In 2005, he obtained an M.Sc. degree in medical physics and clinical engineering with a thesis on the attenuation correction of SPECT for detection of myocardial ischemia. He is currently a Ph.D. candidate in the Department of Mechanical and Manufacturing Engineering of the University of Cyprus, Nicosia, Cyprus. His research interests are in the quantification of

perfusion using contrast enhanced ultrasound.

Mr. Lampakis has co-authored three papers in peer-reviewed journals and conference proceedings.



Vassilis Sboros received a B.Sc. degree in physics from the University of Athens in 1993, an M.Sc. degree in medical physics from the University of Aberdeen in 1994, and a Ph.D. degree in ultrasound contrast imaging from the University of Edinburgh in 1999.

He has worked on the physics of microbubbles and the engineering of imaging them. He has further specialized in nano-sensing techniques using atomic force microscopy. Currently, he is a basic science fellow of the British Heart Foundation at the Medical Physics Department of the University of Edinburgh. His current interests expand to clinical and preclinical ultrasound imaging.

Dr. Sboros published more than 30 articles in international journals and conference proceedings.



Alan McNeilly received a B.Sc. (Hons.) degree in agriculture in 1968 from the University of Nottingham, a Ph.D. degree in endocrinology in 1971 from the University of Reading, and a D.Sc. degree in endocrinology 1984 from the University of Edinburgh.

He is a principal investigator reproductive endocrinologist working at the Medical Research Council Human Reproductive Sciences Unit in Edinburgh. He is also an honorary professor of the

University of Edinburgh. He has a lifelong research interest in how the brain regulates ovarian function, from molecular through cell to whole animal studies. Sheep have been a long-term model and collaborations have extended these studies to the role of the microvasculature in the ovary using contrast-enhanced ultrasound to understand the local endocrine changes vital for normal ovarian function.

Prof. McNeilly is a Fellow of the Royal Society of Edinburgh and chair of the Society for Endocrinology Science Committee. He is the 2008 Dale Medalist of the Society for Endocrinology. Previously, he has served as Editor-in-Chief of the *Journal of Endocrinology*, Chairman of the Society for Reproduction and Fertility, and served on the editorial board of several international journals. He has published more than 400 papers.



Michalakis Averkiou (M'98) received the B.S., M.S. and Ph.D. degrees in 1987, 1989, and 1994, respectively, all in mechanical engineering with specialization in nonlinear acoustics/biomedical ultrasound, from the University of Texas at Austin.

Since 2005, he has been an Assistant Professor in the Department of Mechanical and Manufacturing Engineering of the University of Cyprus, Nicosia, Cyprus. He is also a recipient of a Marie Curie chair of excellence. He was a Postdoctoral

Fellow at the Applied Physics Laboratory of the University of Washington from 1994 to 1996. He worked at Philips Medical Systems R&D department from 1996 to 2005. His research interests are in the areas of diagnostic ultrasound imaging, microbubble ultrasound contrast agents and their applications in oncology, quantification of tumor angiogenesis, therapeutic applications of ultrasound, and ultrasound induced drug delivery.

Prof. Averkiou has authored and co-authored more than 50 journal articles and conference proceedings, and three book chapters. He holds more than 30 U.S. and international patents on diagnostic and therapeutic applications of ultrasound.